Nanoscale

PAPER

View Article Online
View Journal | View Issue

Cite this: *Nanoscale*, 2022, **14**, 8663

Particle nanosizing and coating with an ionic liquid: two routes to improve the transport properties of $Na_3V_2(PO_4)_2FO_2$†

Jacob Olchowka, *[a,b,c] Runhe Fang,[b,d] Rafael Bianchini Nuernberg,[a]
Chloé Pablos,[a,b,e] Dany Carlier,[a,b,c] Sophie Cassaignon*[b,d] and
Laurence Croguennec [a,b,c]

Received 24th February 2022,
Accepted 23rd May 2022

DOI: 10.1039/d2nr01080a

rsc.li/nanoscale

$Na_3V_2(PO_4)_2FO_2$ is a promising candidate for practical use as a positive electrode material in Na-ion batteries thanks to its high voltage and excellent structural stability upon cycling. However, its limited intrinsic transport properties limit its performance at fast charge/discharge rates. In this work, two efficient approaches are presented to optimize the electrical conductivity of the electrode material: particle nanosizing and particle coating with an ionic liquid (IL). The former reveals that particle downsizing from micrometer to nanometer range improves the electronic conductivity by more than two orders of magnitude, which greatly improves the rate capability without affecting the capacity retention. The second approch dealing with an original surface modification by applying an IL coating strongly enhances the ionic mobility and offers new perspectives to improve the energy storage performance by designing the electrode materials' surface composition.

1. Introduction

Human-induced climate problem is already impacting the weather and producing extreme climate in every inhabited region across the world such as frequent heatwaves, heavy precipitation, droughts and tropical cyclones.[1] To face this problem, the main solution is based on limiting the cumulative CO_2 and other greenhouse gas emissions. To do so, one of the major methods is to convert the fossil fuel-based power station, led by coal-fired power plants, into alternative energy like solar and wind energy accompanied by performant energy storage systems, which can store the additional power during peak production periods and supply it to the grid during low hours to reduce burden on the electric grid. Complementary to the widely used lithium ion batteries, sodium ion batteries are environmentally friendly and a reliable choice for large-scale energy storage.[2–5] Among the various families of positive electrode materials, despite weight penalty *versus* layered oxides, polyanionic ones attract much attention thanks to their high average operating potential and structural stability. The most studied and promising are NASICON $Na_3V_2(PO_4)_3$,[6,7] $Na_4MnV(PO_4)_3$,[8,9] $Na_4FeV(PO_4)_3$ [10,11] and vanadium phosphate oxyfluoride series $Na_3V^{3+}_{2-y}V^{4+}_y(PO_4)_2F_{3-y}O_y$ ($NVPFO_y$).[12,13] Dealing with this latter, $Na_3V^{4+}_2(PO_4)_2FO_2$, the most oxidized member of $NVPFO_y$ family, exhibits a slightly lower average working potential than that of $Na_3V^{3+}_2(PO_4)_2F_3$ (~3.8 V *vs.* Na/Na^+ for $NVPFO_2$ *versus* ~3.95 V *vs.* Na/Na^+ for NVPF for a similar capacity).[12,14] However, oxygen for fluorine substitution enhances Na^+ mobility and stabilizes the structure at overcharged states, making $NVPFO_2$ and mixed anionic $NVPFO_y$ still of interest for practical purposes.[12,15]

$Na_3V^{3+}_{2-y}V^{4+}_y(PO_4)_2F_{3-y}O_y$ is composed of $V_2O_{8+y}F_{3-y}$ bi-octahedral units, which are connected by PO_4 groups to generate a three-dimensional structure. Although the robust framework supported by PO_4^{3-} groups leads to stable long cycling capability, the isolated transition metals in this structure result in rather low intrinsic electronic conductivity.[16] Additionally, Notten *et al.* have recently demonstrated that the poor rate performance of NVPF is related to the low Na^+ diffusion coefficient in the material.[17] The authors have shown that hard carbon diffusion coefficient is one order of magnitude higher than that of the polyanionic material. Thus, the $NVPFO_y$ family materials suffer from significant capacity loss

---

[a] *Univ. Bordeaux, CNRS, Bordeaux INP, ICMCB, UMR 5026, F-33600 Pessac, France. E-mail: jacob.olchowka@icmcb.cnrs.fr*
[b] *RS2E, Réseau Français sur le Stockage Electrochimique de l'Energie, CNRS 3459, 80039 Amiens Cedex 1, France*
[c] *ALISTORE-ERI European Research Institute, CNRS 3104, 80039 Amiens Cedex 1, France*
[d] *Sorbonne Université, CNRS, Laboratoire Chimie de la Matière Condensée de Paris, LCMCP, UMR 7574, 4 Place Jussieu, 75005 Paris, France*
[e] *Laboratoire de Réactivité et de Chimie des Solides, Université de Picardie Jules Verne, CNRS-UMR 7314, F-80039 Amiens Cedex 1, France*

† Electronic supplementary information (ESI) available. See DOI: **https://doi.org/10.1039/d2nr01080a**

at high charging/discharging rates. In recent years, numerous methods such as the application of a carbon coating or the formation of composites with carbons (carbon nanotubes, reduced graphene oxides or amorphous carbons),[18–21] partial transition metal substitution (Al, Cr, Mn, Y, Zr, Ga, *etc.*)[22–28] and morphology design (flower, sand rose, nano/micro-sphere, nano/micro-cube, *etc.*)[29–34] have been proposed to overcome this problem. Among the various synthesis methods, morphology control and hybridization with a carbon-based conductive phase are often carried out by hydrothermal/solvothermal synthesis.[34,35] However, this synthesis process leads most often to partial oxidation of vanadium and to a V^{3+}/V^{4+} ratio difficult to be controlled in the final composition, which drastically affects the energy storage performance and thus makes it difficult to evaluate the sole influence of morphology.[34,36–39] Recently, Olchowka *et al.* have reported an original ionothermal synthesis method leading to $NVPFO_2$ particles coated with an EMI TFSI ionic liquid (IL).[40] Their energy storage performance appears promising, even if the effect of IL coating is not fully understood yet.[40]

In this work, $Na_3V_2(PO_4)_2FO_2$ was synthesized by three different methods (solid-state reaction, ionothermal and solvothermal syntheses) to investigate the effects on the electrical properties of particle downsizing and of formation of an ionic liquid coating. For each compound, the final V^{4+} oxidation state, as well as the composition, was meticulously confirmed by combining X-ray diffraction and different spectroscopic characterization methods. The influence of the particle size and IL coating on electronic and ionic conductivities was investigated by electrochemical impedance spectroscopy, whereas electrochemical tests allowed us to evaluate the impact on the energy storage performance.

2. Experimental section

2.1 Material preparation

$NVPFO_2$ materials were synthesized by three different methods. $NVPFO_2$-Iono was obtained by ionothermal synthesis. α-$VOPO_4\cdot 2H_2O$ (homemade) and NaF (molar ratio of 2/3) were placed in a Teflon Parr autoclave with 6 mL of EMI-TFSI (1-ethyl-3-methyl-imidazolium bis(trifluoromethylsulfonyl)imide) and heated at 220 °C for 10 hours, similar to the conditions described in our previous work.[40] The polycrystalline powder was recovered by centrifugation and washed with ethanol. $NVPFO_2$-Nano was obtained by solvothermal synthesis. A stoichiometric mixture of $VO(acac)_2$ (Sigma-Aldrich), NaF (Sigma-Aldrich) and H_3PO_4 (molar ratio of 1/1.5/1) was placed in a 100 mL Teflon Parr autoclave with a mixture of 4.5 mL ethanol/4.5 mL distilled water and heated at 180 °C for 10 hours. $NVPFO_2$-Bulk was prepared by a solid-state reaction of VPO_4 (homemade), $VOPO_4$ (homemade), NaF (Sigma-Aldrich) and Na_2CO_3 (Sigma-Aldrich) taken in a molar ratio of 1 : 1 : 1 : 1, as described earlier.[41] Mechanical grinding was first applied in order to get a homogeneous mixture, and then the resulting powder was pelletized and heated under argon flow in a gold crucible at 550 °C for 2 hours. VPO_4 and $VOPO_4$ were obtained from an α-$VOPO_4\cdot 2H_2O$ homemade precursor. First, α-$VOPO_4\cdot 2H_2O$ was obtained by heating 5 g of V_2O_5 (Sigma-Aldrich) in a mixture composed of 40 mL of phosphoric acid, 110 mL of nitric acid (Sigma-Aldrich) and 130 mL of distilled water at 100 °C for 3 hours. The resulting yellowish powder was washed with acetone. Freshly obtained $VOPO_4\cdot 2H_2O$ was dehydrated at 250 °C under O_2 to produce $VOPO_4$. The latter was then reduced under argon/hydrogen flow at 890 °C for 2 hours to synthesize VPO_4.

2.2 Characterization techniques

X-ray diffraction (XRD) measurements were carried out using a BRUKER D8 ADVANCE diffractometer in θ–θ configuration, equipped with a Cu $K_{\alpha 1,2}$ X-ray source. The acquisition was performed in the 2θ angular range of 10°–140° with a step size of 0.0197°. The Rietveld refinements were performed using the FullProf Suite.[42]

Scanning electron microscopic (SEM) images were acquired without any conductive deposition using a Hitachi Model S-3400N microscope. Gold deposition was made on the $NVPFO_2$-Bulk sample to improve the quality of the images. SEM-FEG (field emission gun) images were obtained using a Hitachi SU-70 microscope. Transmission electron microscopy (TEM) was carried out using a Tecnai spirit G2 microscope. The powder was sonicated for 20 min in ethanol before the analysis.

The chemical analysis of the Na, P and V contents was performed by inductively coupled plasma-optical emission spectroscopy (ICP-OES) using a Varian Model 720-ES spectrometer, after a complete dissolution of the powders into a concentrated hydrochloric acid (HCl) solution.

X-ray photoelectron spectroscopy (XPS) spectra were recorded using an Omicron Argus X-ray photoelectron spectrometer for an applied power of 280 W and a monochromatic Al-Kα radiation source (1486.6 eV). Charge correction was done by calibrating the C 1s peak at a binding energy of 284.8 eV.

Raman spectra were recorded using a confocal LabRAM HR Evolution micro-spectrometer from Horiba, with a 633 nm laser source. They were collected in the range of 100–1300 cm^{-1}, using a 10.6 mm (NA 0.5) focal length lens and with an acquisition time of 20 s and 40 accumulations.

Magic angle spinning nuclear magnetic resonance (MAS NMR) experiments were carried our using standard Bruker 2.5 mm MAS probes at a spinning frequency of 30 kHz. ^{31}P MAS NMR spectra were recorded using a Bruker Avance III 100 MHz spectrometer at a resonance frequency of 40.6 MHz. A Hahn echo sequence was used synchronized with one rotor period rotation, with a 90° pulse of 1.1 μs and a recycle delay of 1 s. H_3PO_4 85% (Sigma-Aldrich) was used as an external reference for 0 ppm chemical shift. ^{23}Na MAS-NMR spectra were recorded using a Bruker Avance 500 MHz spectrometer equipped with an 11.7 T widebore magnet (operating at a Larmor frequency of 132.3 MHz for ^{23}Na). A short pulse length of 1.1 μs corresponding to a selective π/8 pulse determined using a 0.1 M NaCl aqueous solution was employed. Chemical shifts were referenced relative to an aqueous 0.1 M NaCl solution at 0 ppm. The spectral width was set to 1 MHz and the recycle delay of 0.5 s, which was long enough to avoid T_1 saturation effects. The baseline distortions resulting from the spectrometer dead time (5–10 μs) were removed computationally by using a polynomial baseline correction routine.

The electrical properties of $Na_3V_2(PO_4)_2FO_2$ compounds were investigated by electrochemical impedance spectroscopy (EIS). For this purpose, the powders were pressed into pellets of 13 mm diameter applying 200 MPa by means of a uniaxial press. Prior to pressing, $NVPFO_2$-Nano and $NVPFO_2$-Bulk powders were mixed with camphor (about 2 wt%) to provide enough mechanical strength allowing the extraction of the pellets from the die after pressing. Subsequently, the pellets were heat-treated at 250 °C for 1 h under air to evaporate the camphor. Contrary to the two other samples, $NVPFO_2$-Iono could be well pelletized without camphor. Moreover, the evaporation of camphor at 250 °C would decompose the IL. Finally, gold electrodes were sputtered on the parallel and opposite faces of each pellet to ensure electrical contacts. EIS measurements were performed using a Solartron 1260 Impedance/Gain Phase Analyzer in the frequency range between 1 MHz and 1 Hz, with an applied root mean square voltage of 100 mV, 10 points per decade and 20 measures per point. Impedance of all the samples were measured under heating and cooling in air on a two-probe sample holder and over the temperature range of 100–300 °C. Among them, $NVPFO_2$-Iono was left at 300 °C for 6 h to completely remove the IL and then taken for the cooling process.

The electrochemical performance of the materials were tested in CR2032-type coin cells. The cells were assembled in an argon-filled glovebox (H_2O, $O_2 \leq 0.1$ ppm), with sodium metal as the counter electrode. The positive electrodes were prepared as a mixture containing an active material, carbon black, and polyvinylidene fluoride (PVDF) in NMP (*N*-methyl-2-pyrrolidone) in the ratio of 88/7/5 (by wt%). After two hours of thorough mixing, the black ink was casted as a flat film by a doctor blade on an aluminum foil and dried in an oven at 80 °C. Disks were cut, pressed under 5 tons and, finally, dried overnight at 80 °C under vacuum. The electrodes have a typical active mass loading around 4.5–5 mg cm^{-2}. A homemade electrolyte containing a 1 mol L^{-1} solution of $NaPF_6$ (Strem Chemical; 99%) in ethylene carbonate and dimethyl carbonate (EC/DMC = 1/1) with 2 wt% of fluoroethylene carbonate (FEC) was used for all the electrochemical tests. The assembled cells were cycled in a galvanostatic mode, from C/20 to 2C cycling rates between 2.5 and 4.3 V *vs.* Na^+/Na. The theoretical capacity being 130 mA h g^{-1} (corresponding to 2 Na^+ reversibly extracted from $NVPFO_2$), the rate C/20 corresponds to the exchange of 2 Na^+ in 20 hours. Galvanostatic intermittent titration technique (GITT) measurements were performed in half-cells *versus* Na after three cycles of formation at C/20. GITT measurements of $NVPFO_2$ involved a series of 30 min galvanostatic charge/discharge at C/25 followed by relaxation up to 1 mV h^{-1} between 2.5 and 4.3 V to achieve a nearly steady state.

Full cells HC//$NVPFO_2$-Nano were tested in CR2032-type coin cells with a mass ratio of $m(NVPFO_2)/m(HC) \approx 2.35$. The positive electrode possesses a diameter of 16 mm (~9 mg), whereas the negative electrode is slightly smaller (15 mm). The assembled full cells were cycled in the galvanostatic mode, from C/20 to 2C cycling rates (based on $NVPFO_2$ electrode) in the voltage range of 2.5 to 4.3 V and in the same electrolyte, as described previously.

3 Results and discussion

3.1 Structural and morphological characterization

The powder XRD patterns illustrated in Fig. 1 and the Rietveld refinements presented in Fig. S1† confirm that the three synthesis methods (solid-state reaction, solvothermal and ionothermal) lead to the synthesis of the pure $Na_3V^{4+}{}_2(PO_4)_2FO_2$ ($NVPFO_2$) phase. For each compound, all the diffraction peaks could be indexed in the space group $P4_2/mnm$, and the lattice parameters, reported in Table 1, are in good agreement with those of $Na_3V^{4+}{}_2(PO_4)_2FO_2$, the end member composition of the $Na_3V^{3+}{}_{2-y}V^{4+}{}_y(PO_4)_2F_{3-y}O_y$ ($0 \leq y \leq 2$) solid solution.[12,40,43]

Additionally, ICP analyses confirm the expected cationic ratio (Table S1†). A comparison of the X-ray diagrams (Fig. 1) clearly shows differences in the diffraction peak width and preferential orientation, suggesting huge variations in the crystallite size and morphology within the series of $NVPFO_2$. Indeed, compared to observations made for $NVPFO_2$-Nano and $NVPFO_2$-Bulk, the very intense (002) reflection observed for $NVPFO_2$-Iono suggests an oriented particle growth in the (*ab*) plane leading to platelet (2D) morphology. Furthermore, dissimilar diffraction peak broadening, highlighted in the inset of Fig. 1, unveils disparate crystallite sizes caused by the

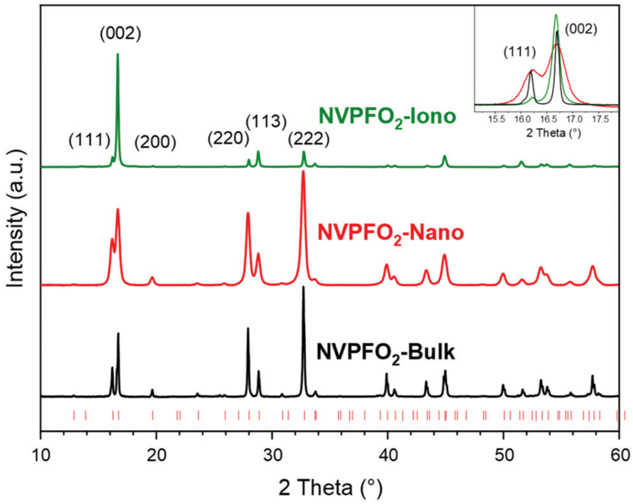

Fig. 1 X-ray diffraction patterns of $NVPFO_2$-Iono (green curve), $NVPFO_2$-Nano (red curve) and $NVPFO_2$-Bulk (black curve). The red ticks correspond to theoretical positions as reported in ICDD 01-083-7199. The inset shows the enlargement of the (111) and (002) reflections.

Table 1 Lattice parameters obtained by the Rietveld refinement of the XRD patterns, coherent domain sizes calculated using the (220) and (002) reflections

	a (Å)	c (Å)	(220) (nm)	(002) (nm)	Space group
$NVPFO_2$-Iono	9.0098(1)	10.6278(1)	52	52	$P4_2/mnm$
$NVPFO_2$-Nano	9.0214(2)	10.6216(3)	23	21	$P4_2/mnm$
$NVPFO_2$-Bulk	9.0330(1)	10.6137(2)	64	70	$P4_2/mnm$

different synthesis conditions. The coherent domains calculated using the Scherrer equation are reported in Table 1, and they reveal that the high-temperature solid state reaction leads to the biggest crystallites (~70 nm), whereas the solvothermal synthesis to the smallest ones (~20 nm). Moreover, the similar coherent domains calculated with the (002) and (220) reflections suggest an isotropic crystal growth for all synthesis routes, despite an anisotropic particle growth by the ionothermal reaction. Finally, the internal strains generated by limited crystallite sizes distributed within the oriented primary particles result in difficulties to perfectly fit the peak profile during structural refinement, which could explain the slightly different lattice parameters within the $NVPFO_2$ series (Table 1 and Fig. S1†). Consequently, the chemical composition has to be confirmed by local environmental characterization techniques such as ss-NMR, as it will be done later.

SEM, SEM-FEG (Fig. 2) and TEM images (Fig. S2†) further confirm the various morphologies of $NVPFO_2$ materials obtained by the different synthesis methods. $NVPFO_2$-Iono, which was obtained by a topochemical reaction from layered α-$VOPO_4·2H_2O$,[40] was characterized by aggregated flakes with an average length of around 5–10 μm and a thickness of 100–200 nm (Fig. 2a, b and S2†). The small fragments that can be distinguished probably come from pieces of big flakes. HRTEM analyses further revealed that the platelets exhibit the (220) crystallographic planes through lattice fringes obser-

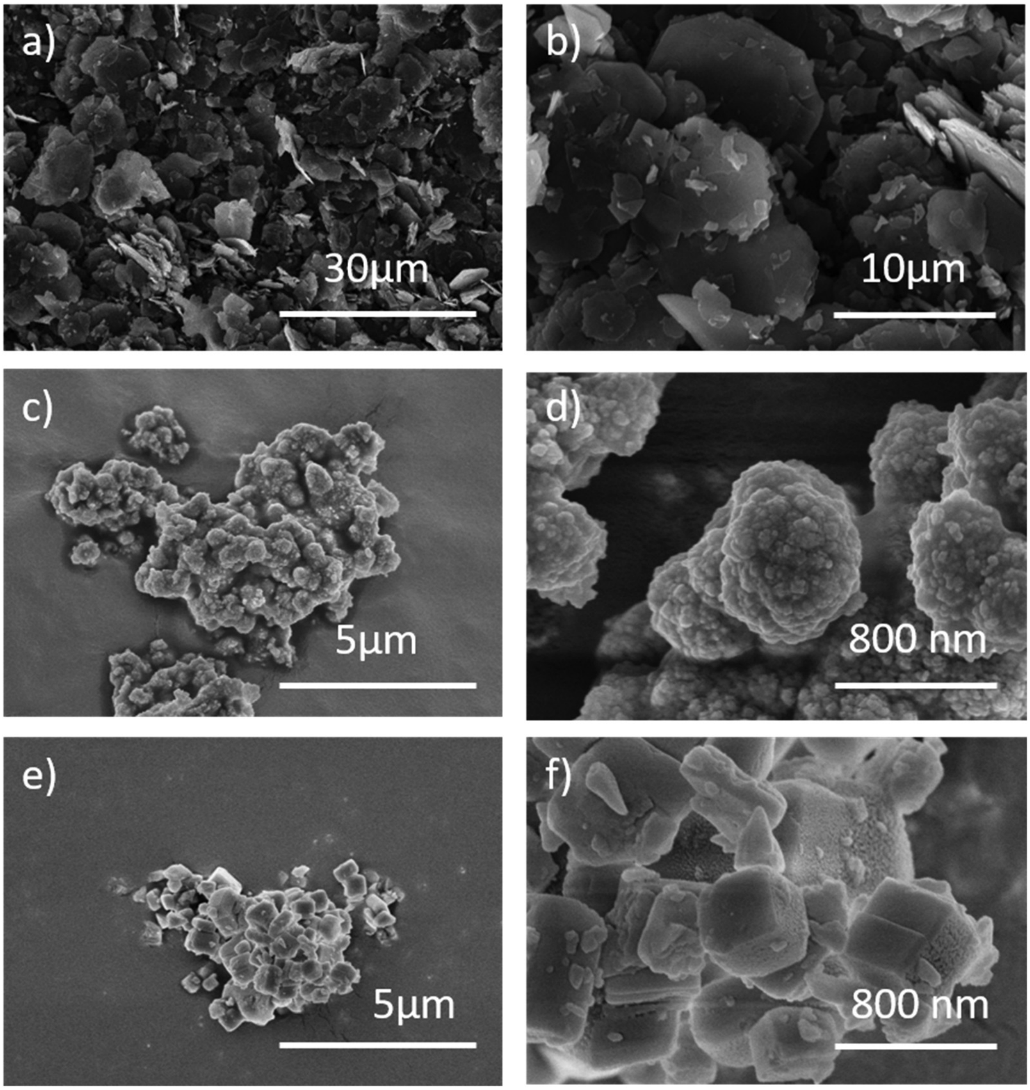

Fig. 2 (a and b) SEM images of $NVPFO_2$-Iono. (c and d) SEM-FEG images of $NVPFO_2$-Nano. (e and f) SEM-FEG images of $NVPFO_2$-Bulk.

vation (Fig. S3a and b†), which perfectly fit to the exalted intensity of the (002) diffraction peak observed by XRD. Thus, it can be concluded that the Na^+ diffusion channels along the [110] and [$1\bar{1}0$] directions are situated in the plane of the flakes (Fig. S4†). $NVPFO_2$-Nano synthesized by a solvothermal process presents a quite different morphology (Fig. 2c and d). It was characterized by aggregates made of randomly agglomerated spherical secondary particles of diameter ~ 500 nm. These latter were constructed with smaller primary particles of size around 30 nm, which is in good agreement with the crystallite size determined by XRD (Table 1). The different lattice fringes observed by HRTEM (Fig. S3†) for $NVPFO_2$-Nano (0.32 nm (220), 0.53 nm (002) and 0.55 nm (111)) support the spherical morphology of the small primary particles and the absence of preferential orientation. Finally, the shape of $NVPFO_2$-Bulk obtained by the high-temperature solid-state reaction approximates to cubes varying from hundreds of nanometers to several micrometers (Fig. 2e and f). Moreover, the thickness of $NVPFO_2$-Bulk cubes makes the lattice fringe measurement impossible.

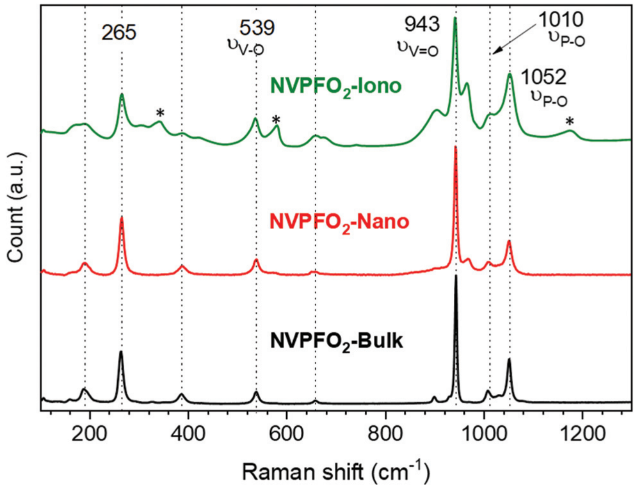

Fig. 3 Raman spectra of $NVPFO_2$-Iono (green), $NVPFO_2$-Nano (red) and $NVPFO_2$-Bulk (black). The band marked with a star on the Raman spectrum corresponds to the EMI TFSI ionic liquid.

The series of $NVPFO_2$ was further characterized by various spectroscopic techniques to probe the Na, P and V local environments and confirm the composition deduced from Rietveld refinements. As illustrated in the Raman spectra in Fig. 3, all materials possess the typical signature of $Na_3V_2(PO_4)FO_2$ with peaks at 539 cm^{-1}, 943 cm^{-1}, 1010 cm^{-1} and 1052 cm^{-1} attributed to the vibrations of V–O, V=O and phosphate groups respectively.[39,44,45] As reported in our previous work on the topochemical reaction mechanism happening during the ionothermal synthesis of $NVPFO_2$, the ionic liquid functionalizes the particle surface to create an IL coating, which can be seen as an "artificial solid electrolyte interface".[40] This latter, which in some cases stabilizes the electrode material upon cycling and favors ionic adsorption on the surface and/or alkaline diffusion through the material,[46–48] is observed on the $NVPFO_2$-Iono spectrum (Fig. 3) and on HRTEM images (Fig. S5†). Indeed, the band marked with a star on the Raman spectrum is in rather good agreement with those expected for the EMI TFSI ionic liquid.[49–52] IL can also be detected on the surface of $NVPFO_2$-Iono by XPS analysis that reveals the presence of N 1s and S 2p peaks originating from the imidazolium ring and TFSI respectively (as shown by the surveys in the energy range of 0–1100 eV in Fig. S6† and by the quantification given in Table S2†). Meanwhile, the F 1s spectra (Fig. 4a) clearly show a signal at 684.1 eV for all the compounds, corresponding to fluorine in the polyanionic materials, whereas $NVPFO_2$-Iono presents a second peak at 688.6 eV, which is in agreement with the presence of CF_3 from EMI TFSI.[47,53,54] However, this IL coating does not seem to affect the inorganic core phase. The V 2p XPS spectra of the $NVPFO_2$ series are presented in Fig. 4b, and the spectrum of each compound exhibits two broad peaks at 517.3 eV and 524.8 eV corresponding to the V $2p_{3/2}$ and V $2p_{1/2}$ transitions. These binding energies are consistent with the expected ones for this polyanionic material with the V^{4+} environment and

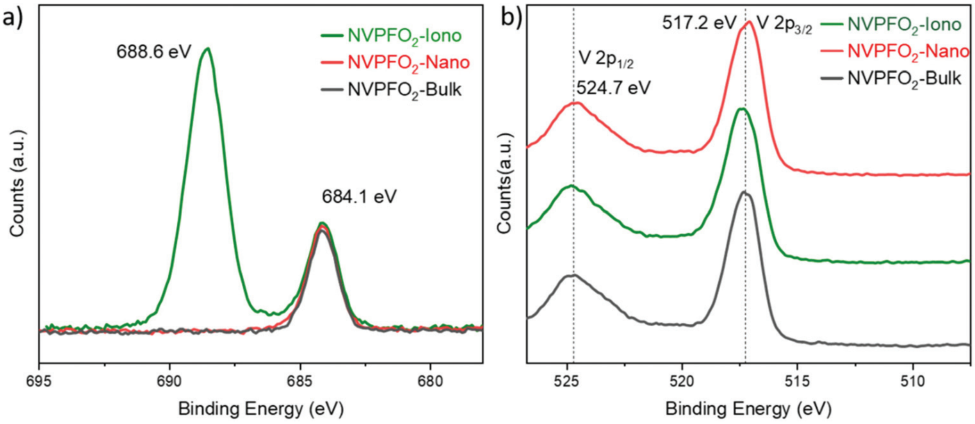

Fig. 4 (a) F 1s XPS spectra and (b) V 2p XPS spectra for all the $NVPFO_2$ materials.

demonstrate for NVPFO$_2$-Iono that the IL coating does not affect the electronic structure of vanadium present near the surface.[55]

For all compounds, the ^{23}Na ss-NMR spectrum (Fig. 5a) reveals a main peak at ~77 ppm, whose position is mainly due to the hyperfine interaction between the Na$^+$ nucleus and the unpaired electron of paramagnetic V^{4+} ions and is characteristic of the Na(OV^{4+})$_2$ environment.[12,56] The absence of signals at a higher isotropic shift confirms the absence of V^{3+} in these phases and validates the Na$_3$V$^{4+}{}_2$(PO$_4$)FO$_2$ composition.[14,36,41,56] Meanwhile, the broader signal for NVPFO$_2$-Nano could be the consequence of disorder due to particle downsizing.[34] ^{31}P ss-NMR spectra obtained for all NVPFO$_2$ show a very intense signal at ~0 ppm corresponding to the P(OV^{4+})$_4$ local environment (Fig. 5b).[56] Once again the absence of signals induced by the Fermi contact shift at ~1500, 3000 ppm, 4500 ppm or 6000 ppm, as previously observed for the Na$_3$V$_2$(PO$_4$)$_2$F$_{3-y}$O$_y$ series, excludes the existence of V^{3+} in the compounds.[22,56] The enlarged area in Fig. 5c unfolds more details on the signal located around 0 ppm. Three distinct signals are observed for NVPFO$_2$-Bulk that most probably correspond to the inequivalent local environments for the phosphorus. However, the signals of NVPFO$_2$-Nano and NVPFO$_2$-Iono are broader, asymmetric and less resolved due to the small changes on the local environment brought by the nanosizing/specific morphology.[57] Therefore, the use of different synthesis methods allows to obtain Na$_3$V$^{4+}{}_2$(PO$_4$)FO$_2$ materials with extremely different particle size, with and without coating, thus offering an ideal series to study the particle downsizing and IL coating effects on the transport properties and energy storage performance.

3.2 Transport kinetics and energy storage performance

The energy storage performance of the three Na$_3$V$_2$(PO$_4$)$_2$FO$_2$ samples was first evaluated by cyclic voltammetry and galvanostatic measurements in the half-cell configuration. The electrode formulation (88 wt% active material/7 wt% carbon black/5 wt% PVDF) and the mass loading of ~5 mg cm^{-2} were expected to emphasize on the influence of different NVPFO$_2$ electrode materials. Fig. 6a–c shows the galvanostatic charge–discharge curves obtained within the potential window 2.5–4.3 V *vs.* Na$^+$/Na at different current intensities, whereas the reversible capacity evolution depending on the C-rate is represented in Fig. 6d. All electrode materials exhibit two reversible plateaus or pseudo-plateaus at around 3.6 and 4 V *vs.* Na$^+$/Na, attributed to the V^{5+}/V^{4+} redox couple that is activated by reversible Na$^+$ extraction and in perfect agreement with the values reported in the literature.[12,58] Sharma *et al.* reported that the reaction mechanisms upon charge and discharge are composed of first-order transitions (two-phase transition) separated by second-order ones (solid solution).[59] At C/20, NVPFO$_2$-Nano and NVPFO$_2$-Iono exhibit similar reversible high capacities (~115 mA h g^{-1} and ~110 mA h g^{-1} respectively), close to the theoretical one (130 mA h g^{-1}). However, NVPFO$_2$-Nano possesses a much better capacity retention when the

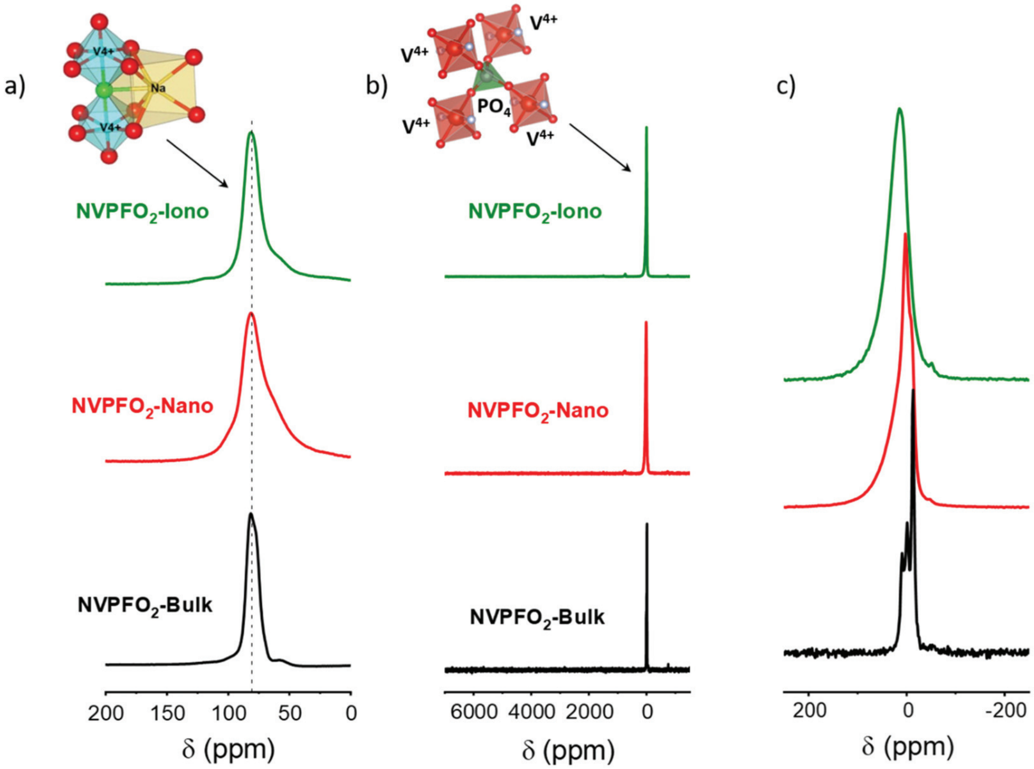

Fig. 5 (a) ^{23}Na solid-state MAS NMR spectra of NVPFO$_2$-Iono (green), NVPFO$_2$-Nano (red) and NVPFO$_2$-Bulk (black). (b) Corresponding ^{31}P solid-state MAS NMR spectra. (c) Enlargement of the signals around 0 ppm.

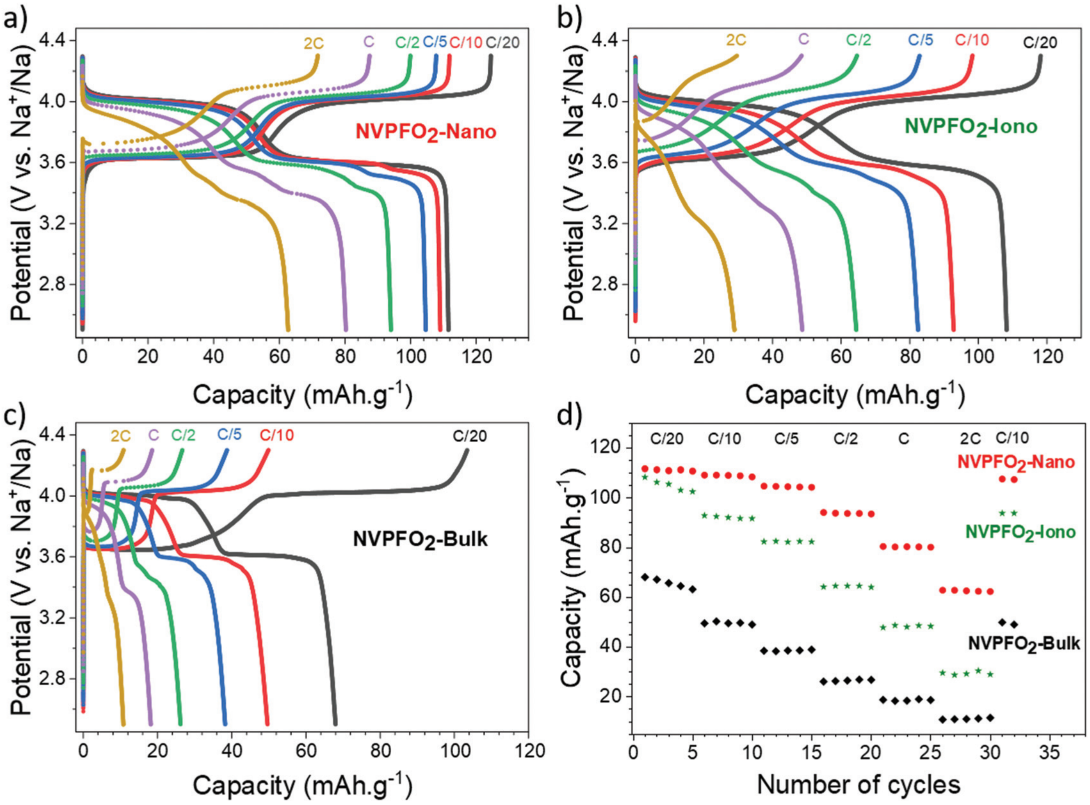

Fig. 6 (a–c) Charge and discharge curves of all the $NVPFO_2$ materials at different cycling rates. (d) Rate capabilities obtained for all these materials, from C/20 to 2C.

charge rate increases up to 2C. Meanwhile, the discharge capacity of $NVPFO_2$-Bulk already merely reaches 67 mA h g^{-1} at C/20 and quickly drops when the current becomes higher. The full initial capacity recovering after several cycles of fast charge/discharge clearly shows that the difference in performance mainly originates from the kinetics limitations specific to the electrode material.

This is supported by the evolution of polarization when the charge rate increases, as illustrated in Fig. 7, which shows the first derivative curves of the 2nd galvanostatic cycle (Fig. 6) performed at C/20 and C/5.

At C/20, the average discharge redox potentials for all electrode materials are observed at 4 V and 3.6 V *vs.* Na^+/Na. These potentials remain unchanged for $NVPFO_2$-Nano when the charge rate increases to C/5, whereas the values drop to 3.98 V and 3.57 V for $NVPFO_2$-Iono and 3.97 V and 3.52 V for $NVPFO_2$-Bulk. Similarly, the ΔE_p (potential difference between charge/discharge) increases for $NVPFO_2$-Iono and more significantly for $NVPFO_2$-Bulk, which leads to a system with slower kinetics, lower average discharge potential and, thus, lower energy density. This clearly shows that the resistance R (sum of electrical and ionic resistances) follows the trend $R_{Bulk} > R_{Iono} > R_{Nano}$ and, thus, strongly depends on the active material, as it is the only variable parameter in this electrode series. Therefore, the transport properties were further investigated to get a deeper insight into the influence of the particle size and IL coating.

The complex impedance data of all the $NVPFO_2$ compounds reveal quite distinct electrical behaviors. Fig. 8 depicts the complex impedance plots of each $NVPFO_2$ sample recorded at 200 °C under heating, and also upon cooling for $NVPFO_2$-Iono. Here, the complex impedance data (Z^*) have already been normalized regarding the shape factor (l/A, thickness over area) of each sample, according to the relation $Z_s^* = Z^*A/l$ giving rise to the specific impedance (Z_s^*). This approach allows a straight comparison between the impedance responses of samples. For samples $NVPFO_2$-Nano (Fig. 8a) and $NVPFO_2$-Bulk (Fig. 8b), the overall electrical resistivity can be promptly read at the low-frequency intercept of the impedance data with the real part of the specific impedance (Z_s'). Thus, sample $NVPFO_2$-Bulk is about one order of magnitude more resistive than sample $NVPFO_2$-Nano. Indeed, sample $NVPFO_2$-Bulk is so resistive that its overall impedance is out of the equipment impedance range at this temperature, thus explaining the dispersion of impedance data in the low-frequency range. A common feature between the electrical behaviors of these samples is the distorted semi-circles probably caused by a joint contribution of grains and grain boundaries in the high- and middle-frequency ranges, respectively.[39] In contrast, $NVPFO_2$-Iono (Fig. 8c) presents an impedance response completely different from that of the other samples and even less resistive than that of the sample $NVPFO_2$-Nano. Its impedance response combines a high-frequency semicircle probably linked to the

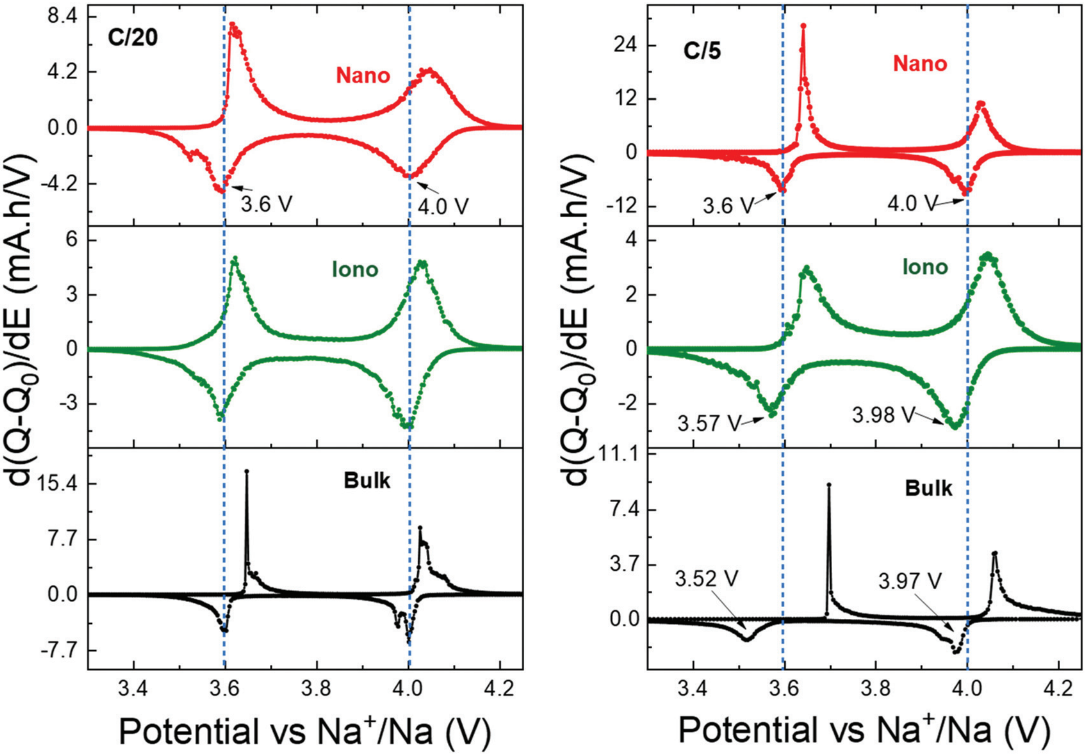

Fig. 7 First derivative curves of the second cycle of galvanostatic charge discharge process of all the NVPFO$_2$ materials at C-rates of C/20 and C/5.

ionic transport enhanced by the IL coating and a low-frequency highly depressed semicircle due to the electrode polarization phenomenon. In theory, if the ionic liquid is rigidly attached onto the surface of NVPFO$_2$ particles and only Na$^+$ ions are mobile, a steep increase of the imaginary part of the impedance should take place in low-frequency range.[47] Since this is not the case, we hypothesized that the ionic molecular species that constitute the ionic liquid could also be relatively mobile either because they are not grafted or because of the high temperature employed for the impedance spectroscopy measurements. In any case, the dependence of the real part of permittivity on frequency reveals a logarithmic increase in the relative permittivity in the low-frequency range typical of an ion blocking effect, precluding the hypotheses of a majority electronic contribution to the overall charge transport (Fig. S7†). Therefore, the electrical resistivity related to the Na$^+$ transport can be roughly read at the middle-frequency real-part projection of the specific impedance (Z_s') between the two semicircles. Furthermore, once this sample is heated up to 300 °C and then cooled down, its electrical behavior changes entirely (Fig. 8d) due to the degradation of the IL, whereas the electrical conductivity is nearly the same upon heating and cooling for the two other electrode materials (Fig. 9). In this case, the final electrical behavior of NVPFO$_2$-Iono is much like that of NVPFO$_2$-Bulk, highly resistive and with two impedance contributions likely coming from grain and grain boundary contributions. The polarization phenomenon caused by the grain boundaries and the ion blocking effect can be visualized respectively as a middle-frequency pseudo plateau and low-frequency logarithmic increase of the real part of permittivity (Fig. S7†).

The dependence of the overall electrical conductivity on the inverse of the temperature was plotted by applying the linearized form of the Arrhenius-like relation (eqn (1)), which is mostly used for ionic conductors but sometimes also applied for electronic conductors:[60–62]

$$\sigma T = \sigma_0 \exp\left(\frac{-E_a}{k_B T}\right) \quad (1)$$

where σ_0 is the pre-exponential factor, E_a the activation energy for ionic conductivity, k_B the Boltzmann constant, and T the absolute temperature. Following this methodology, the linear fit slope is proportional to the activation energy, which therefore provides access to the energetic barrier of the mechanism responsible for the electrical transport.[62] Fig. 9 exhibits the Arrhenius-like plots of the overall electrical conductivity of the NVPFO$_2$ compounds synthesized under different conditions. Overall, the dependence of the electrical conductivity on temperature for NVPFO$_2$-Nano seems to present a low (T < 180 °C) and a high (T > 180 °C) temperature regime, due to the dominating electronic transport at low temperatures and the mixed ionic–electronic conducting behavior at higher temperatures.[39] The activation energy of the high-temperature regime is considerably higher than that of the low-temperature one (Fig. 9). Two activation energy regimes have also been visualized for

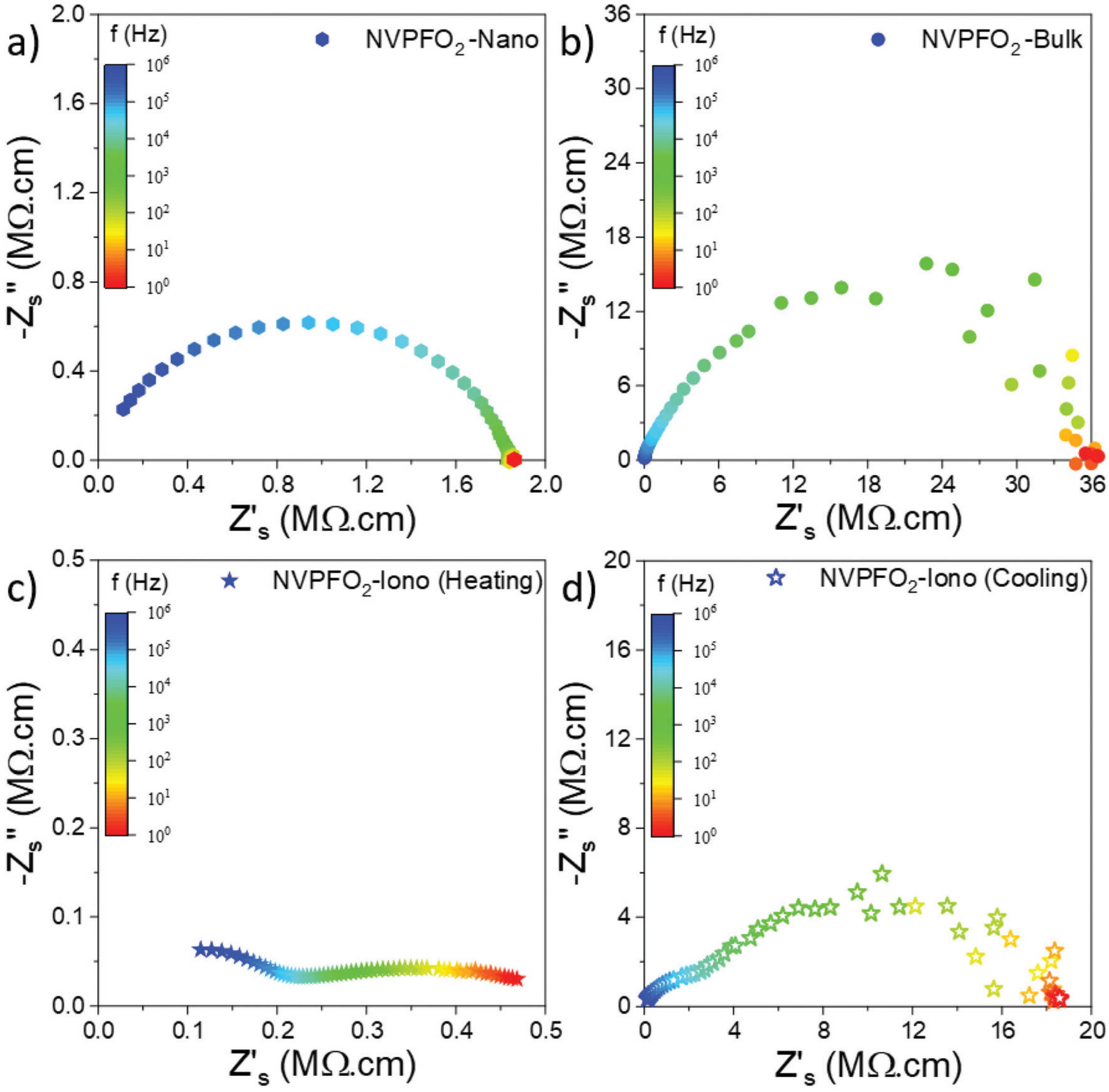

Fig. 8 EIS analyses of $Na_3V_2(PO_4)_2FO_2$ samples recorded at 200 °C under heating for NVPFO$_2$-Nano (a) and NVPFO$_2$-Bulk (b) as well as for NVPFO$_2$-Iono under heating (c) and under cooling (d). The complex impedance data shown here have already been normalized regarding the shape factor of each sample for comparison purposes.

the micrometric NVPFO$_1$ compound reported in the literature by Broux *et al.*[63] Nevertheless, in that case, the transition took place at a temperature around 130 °C and was attributed to a structural change. Besides, in the low temperature regime, this micrometric NVPFO$_1$ compound (obtained by solid-state synthesis) shows much lower conductivity and higher activation energy than NVPFO$_2$-Nano studied in this work (Fig. 9). For example, the conductivity and activation energy for the NVPFO$_1$ reference are ~10^{-10} S cm^{-1} and 0.86 eV at 95 °C, while they are 3×10^{-8} S cm^{-1} and 0.43 eV for NVPFO$_2$-Nano at 100 °C.[63] Likewise, NVPFO$_2$-Bulk in this study also presents an electrical conductivity much lower and an activation energy higher than those of the NVPFO$_2$-Nano compound. Thus, this result indicates the strong enhancement of electronic conductivity induced by particle downsizing.

The sample coated with the IL shows at low temperatures an overall conductivity even higher than that of nanometric NVPFO$_2$ (2.7×10^{-7} S cm^{-1} *vs.* 3×10^{-8} S cm^{-1} at 100 °C) and a similar activation energy within errors of ~0.45 eV. However, above 220 °C, the conductivity drops considerably probably due to the IL decomposition. After six hours at 300 °C, the conductivity of the sample gradually decreases upon cooling to values two orders of magnitude smaller than those observed upon heating (Fig. 9). The activation energy is almost doubled compared with that observed under heating, suggesting a totally different conduction mechanism. Meanwhile, the electrical conductivity of NVPFO$_2$-Iono under cooling is in the same order of magnitude of that observed for NVPFO$_2$-Bulk with similar activation energies of ~0.85 eV, which indicates the strong ionic conductivity improvement brought by IL

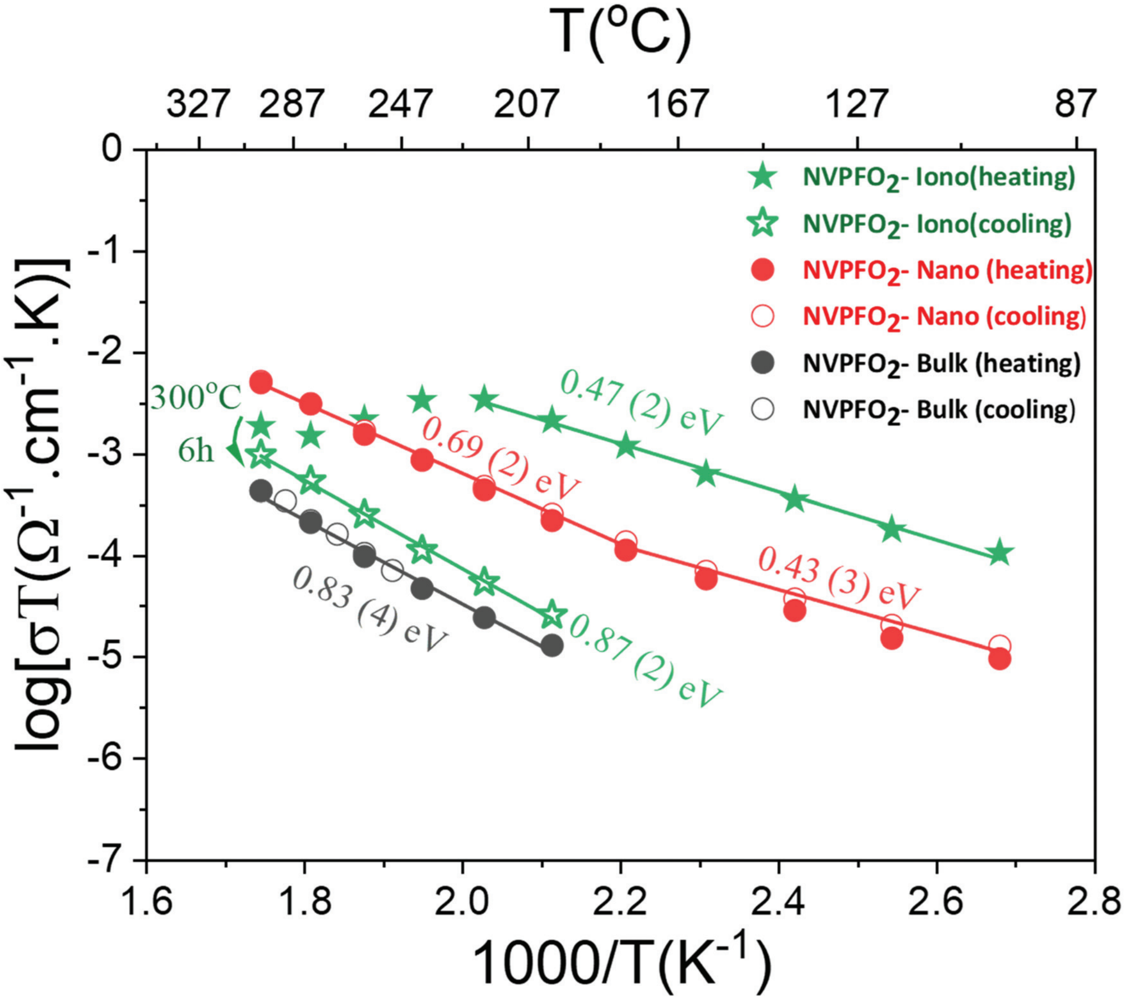

Fig. 9 Arrhenius-like plots of the dependence of the overall electric conductivity on the inverse temperature for $NVPFO_2$ samples synthesized under different conditions.

coating. Barpanda *et al.* have demonstrated a lithium conductivity enhancement by IL grafting on lithium fluoride sulfate compounds,[47] thus in our case Na^+ conductivity in $NVPFO_2$-Iono would be strongly improved.

The Na^+ diffusion during redox reactions was investigated through the CV analysis at different scan rates from 0.025 mV s^{-1} to 0.8 mV s^{-1} in the potential range between 2.5 V and 4.3 V *vs.* Na^+/Na to avoid possible electrolyte degradation (Fig. 10a–c). Two oxidation and two reduction peaks, representing respectively the two plateaus in galvanostatic charge and discharge curves, are observed for all the $NVPFO_2$ materials. Interestingly, at high scan rates, the two oxidation and reduction peaks strongly overlap for $NVPFO_2$-Iono, which suggests the absence of Na^+ ordering and a single-phase reaction mechanism. This could be explained by the enhanced Na^+ conductivity determined by impedance spectroscopy. Furthermore, the overlap is globally less pronounced for $NVPFO_2$-Nano and even less for $NVPFO_2$-Bulk, which, for instance, exhibits two well-defined reduction peaks for all scan rate ranges. Fig. 10d and Fig. S8† depict the evolution of the peak current intensity (i_p) *versus* the square root of the scan rate ($\nu^{1/2}$) that allows to estimate Na^+ diffusion coefficients using the Randles–Sevcik equation (ESI Part S8† and Table 2).

Nanospherical $NVPFO_2$-Nano reveals the best diffusion capability of 4.06×10^{-11} cm^2 s^{-1} at the O_2 oxidation peak, nearly one order of magnitude higher than the cubic $NVPFO_2$-Bulk with a calculated diffusion coefficient of 5.73×10^{-12} cm^2 s^{-1}. Quite surprisingly, IL-coated $NVPFO_2$ exhibits only an intermediate diffusion coefficient during redox reactions (*e.g.* 1.32×10^{-11} cm^2 s^{-1} for higher potential Na^+ extraction), whereas a high ionic mobility is measured by impedance spectroscopy. It is thus possible that the ionic liquid coating only enhances the Na^+ mobility on the surface of the electrode material and at grain boundaries. During electrochemical impedance spectroscopy measurements, NaTFSI can be formed at the surface of $NVPFO_2$-Iono, while the cationic part of the ionic liquid attached on the $NVPFO_2$ surface transfers its charge to an inorganic material.[64] Thus, the measured conductivity would be that of Na^+ in the IL coating. However, this coating does not affect the Na^+ diffusion in the bulk of the

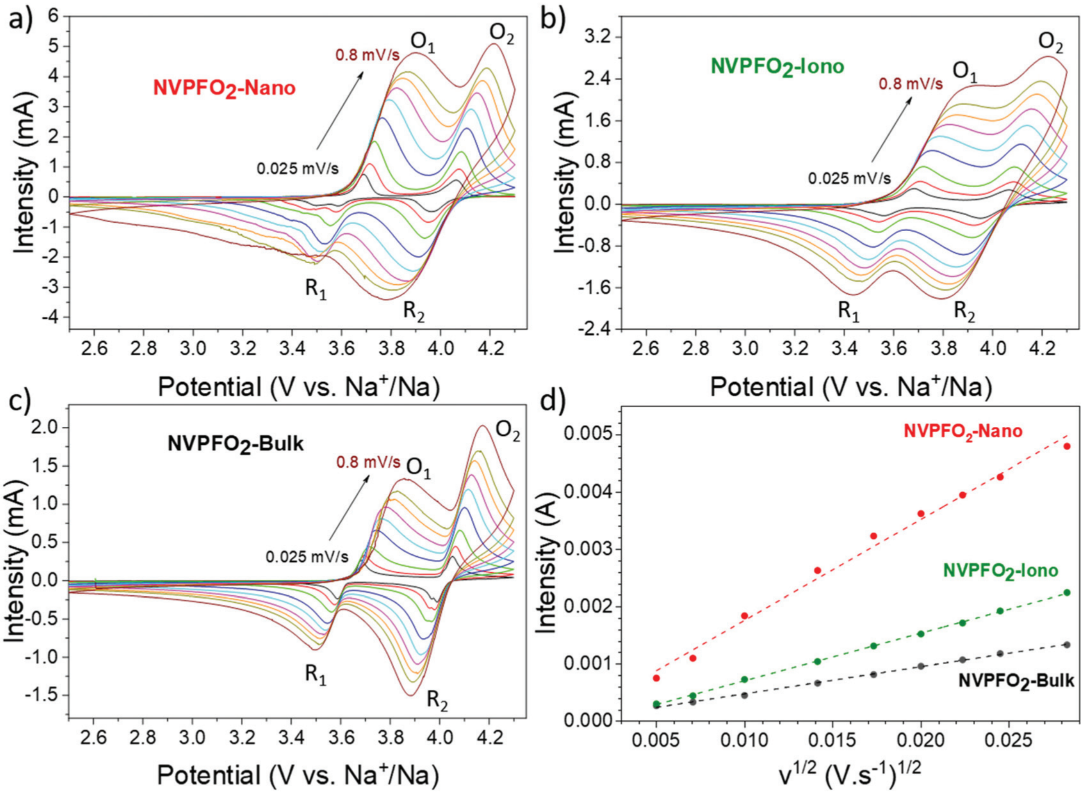

Fig. 10 (a–c) CV curves at different scan rates and (d) the corresponding linear fitting curves between the maximum current (i_p) and the square root of the scan rate ($v^{1/2}$) for the O_1 peak of each compound.

$NVPFO_2$ material. Thus, Na^+ diffusion during oxidation/reduction (CV or galvanostatic charge/discharge) is still limited by solid-state diffusion within the bulk of $NVPFO_2$. Na^+ extraction or insertion necessarily involves an electron transfer to compensate the charge (vanadium oxidation or reduction), and as the electronic conductivity of micrometric $NVPFO_2$ is very low, this limits the intercalation/extraction processes and thus Na^+ diffusion. Besides, GITT measurements confirm this trend, as detailed in ESI Parts S8 and S9.†

Table 2 Diffusion coefficients calculated from CV curves using the Randles–Sevcik equation

D (cm^2 s^{-1})	$NVPFO_2$-Nano	$NVPFO_2$-Iono	$NVPFO_2$-Bulk
O_2	4.06×10^{-11}	1.32×10^{-11}	5.73×10^{-12}
O_1	3.28×10^{-11}	7.67×10^{-12}	2.43×10^{-12}
R_2	1.78×10^{-11}	5.16×10^{-12}	3.10×10^{-12}
R_1	1.73×10^{-11}	4.66×10^{-12}	1.08×10^{-12}

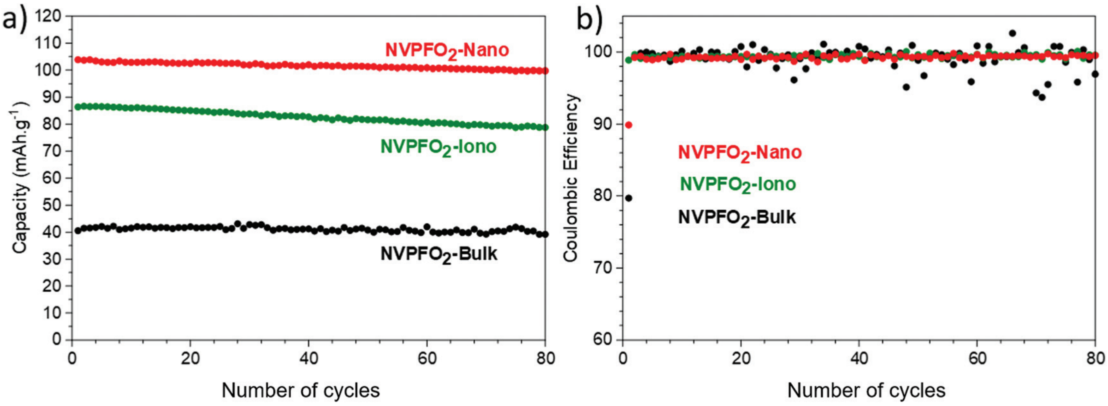

Fig. 11 (a) Evolution of reversible capacity upon long-term cycling at C/5 and (b) related coulombic efficiency of all the $NVPFO_2$ materials.

According to Fig. 11a, all the positive electrode materials reveal good reversible capacity retentions after 80 cycles at C/5. Overall, all $NVPFO_2$ possess stable capacity retention showing that particle downsizing and IL coating does not lead to electrode degradation or irreversible reaction that can be detrimental to practical application. However, the coulombic efficiency of $NVPFO_2$-Bulk is not stable (Fig. 11b). Starting from the 20th cycle, the positive electrode suffers frequent coulombic efficiency loss that might be due to the electrolyte degradation, electric noise or the contact problem in the coin cell. However, its worse electrochemical performance than $NVPFO_2$-Iono and $NVPFO_2$-Nano at this charge and discharge rate emphasizes the benefits of nanosizing and surface coating.

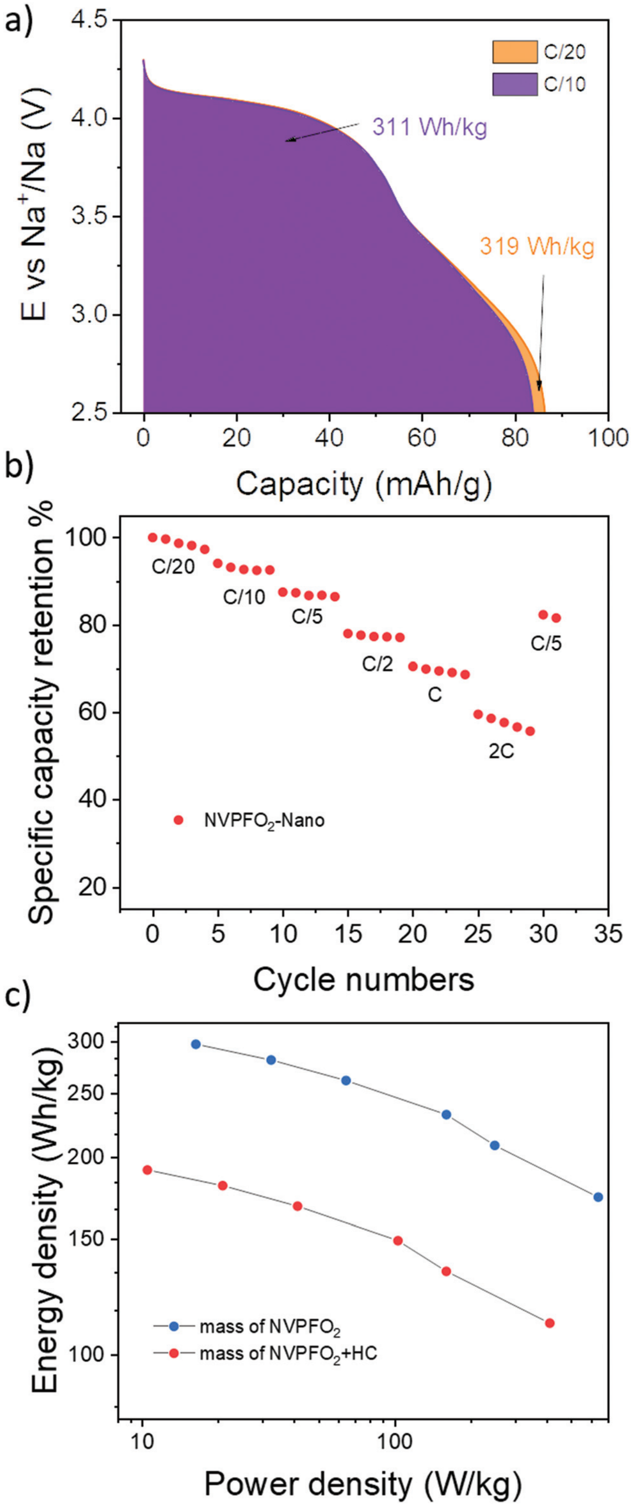

Fig. 12 (a) Energy density calculated for $NVPFO_2$-Nano at C/20 and C/10. (b) Specific capacity retention in % upon increasing the C-rate. (c) Ragone plots of the $NVPFO_2$-Nano full cell; the blue points correspond to the capacity calculated based on the $NVPFO_2$ mass and the red points on both electrode masses.

Bearing in mind the very promising performance obtained for nanospherical $NVPFO_2$, a full cell $NVPFO_2$-Nano *versus* hard carbon was assembled and tested. Considering the electrode composition (88% active material/7% C/5% PVDF), the full cell shows excellent performance with an energy density of 320 W h kg^{-1} at C/20 and 310 W h kg^{-1} at C/10 (Fig. 12a). For comparison, Iarchuk *et al.* reported the same energy density for $NVPFO_2$ but with electrode loadings containing only 70% of active material.[65] Moreover, the full cell still exhibits 70% of its initial capacity at 1C (Fig. 12b). The Ragone plot given in Fig. 12c demonstrates the variation in energy density along with the increase in power density. Compared to a recent study reported by Notten *et al.*, $NVPFO_2$-Nano displays a similar high-rate performance in full cells to an optimized carbon-coated NVPF,[17] which validates the extremely promising performance of our electrode nano-material. Meanwhile, the long-term cycling stability of full cells needs further optimisation as the capacity retention remains limited around 70% after 56 cycles (Fig. S11†). A better balancing between positive and negative electrode masses and other optimisations such as electrolyte formulation would allow us to improve the long-term capacity retention.

4. Conclusion

In summary, $NVPFO_2$ electrode materials have been synthesized by three different synthesis methods, leading to a series of $NVPFO_2$ with different characteristics, which allows the investigation of particle size impact and the effect of an IL coating on the electronic conductivity, diffusion capacity of Na^+ and the energy storage performance separately. A set of spectroscopic characterizations (NMR, XPS and Raman) confirm the $Na_3V_2(PO_4)_2FO_2$ composition for each compound and reveal that the ionic liquid coating on $NVPFO_2$-Iono does not affect the vanadium nor the sodium local environment. Electrochemical impedance spectroscopy measurements demonstrate that particle downsizing improves the electronic conductivity by more than two orders of magnitude in the low temperature range, whereas the IL coating strongly enhances the ionic mobility. For instance, $NVPFO_2$-Nano and $NVPFO_2$-Iono present electrical conductivities around 3×10^{-8} S cm^{-1} and 2.5×10^{-7} S cm^{-1} at 100 °C, whereas the one of $NVPFO_2$-Bulk is estimated below 10^{-10} S cm^{-1}. The broad and overlapping redox peaks on CV curves for $NVPFO_2$-Iono, in addition to the slopping profile on GCD curves, suggest the absence of Na^+ ordering during cycling which may be due to the enhanced ionic mobility caused by the IL coating. Moreover, when $NVPFO_2$-Iono loses its IL coating upon thermal degradation, the conductivity and activation energy become similar to those of $NVPFO_2$-Bulk, which confirms the beneficial role of IL coating. Concerning energy storage performance, $NVPFO_2$-Nano demonstrates the best rate capacity retention, confirming that a good electronic conductivity of positive electrode materials is primordial for high rate cycling, and its absence cannot be fully compensated by improving the ionic diffusion. Besides, $NVPFO_2$-Nano performance in full cells is very promising considering the absence of carbon-coating or formulation optimization. Finally, it was shown that particle downsizing strongly increases the electronic conductivity, whereas an ionic liquid coating enhances the ionic mobility, thus the next step would be to combine both approaches to develop a more performant electrode material.

Author contributions

The manuscript was written by J. O., R. F., R. B. N., S. C. and L. C. through support of all the co-authors. The study was conceptualized by J. O., S. C. and L. C. The synthesis of the different materials were done by R. F. J. O. and C. P.; R. B. N. performed all the electrochemical impedance spectroscopy measurements and analyzed the data; C. P. prepared all the electrode as well as the half and full cells; D. C. performed ss-NMR acquisitions and did data interpretation. Raman measurements and interpretation were done by J. O.

Conflicts of interest

The authors declare no conflicts of interest.

Acknowledgements

The authors thank the Materials Physics and Chemistry Doctoral School (ED397) of Sorbonne University for the funding of Runhe Fang's PhD thesis, as well as the financial support of Région Nouvelle Aquitaine, of the French National Research Agency (STORE-EX Labex Project ANR-10-LABX-76-01 and the Project Nano-INSPIRE ANR-21-CE50-0006) and of the European Union's Horizon 2020 research and innovation program under grant agreement no. 875629 (NAIMA project). The authors also thank Emmanuel PETIT, Cathy DENAGE, Eric LEBRAUD (ICMCB) for their technical support.

References

1 IPCC Working Group I, *Climate Change 2021: The Physical Science Basis*, 2021.
2 Y. Hu, S. Komaba, M. Forsyth, C. Johnson and T. Rojo, *Small Methods*, 2019, **3**, 1900184.
3 I. Hasa, S. Mariyappan, D. Saurel, P. Adelhelm, A. Y. Koposov, C. Masquelier, L. Croguennec and M. Casas-Cabanas, *J. Power Sources*, 2021, **482**, 228872.
4 J.-M. Tarascon, *Joule*, 2020, **4**, 1616–1620.
5 K. M. Abraham, *ACS Energy Lett.*, 2020, 3544–3547.
6 J.-N. Chotard, G. Rousse, R. David, O. Mentré, M. Courty and C. Masquelier, *Chem. Mater.*, 2015, **27**, 5982–5987.
7 C. V. Manohar, A. Raj K, M. Kar, M. Forsyth, D. R. MacFarlane and S. Mitra, *Sustainable Energy Fuels*, 2018, **2**, 566–576.
8 W. Zhou, L. Xue, X. Lü, H. Gao, Y. Li, S. Xin, G. Fu, Z. Cui, Y. Zhu and J. B. Goodenough, *Nano Lett.*, 2016, **16**, 7836–7841.
9 F. Chen, V. M. Kovrugin, R. David, O. Mentré, F. Fauth, J.-N. Chotard and C. Masquelier, *Small Methods*, 2019, **3**, 1800218.
10 S. Park, J. N. Chotard, D. Carlier, I. Moog, M. Courty, M. Duttine, F. Fauth, A. Iadecola, L. Croguennec and C. Masquelier, *Chem. Mater.*, 2021, **33**, 5355–5367.
11 C. Xu, J. Zhao, E. Wang, X. Liu, X. Shen, X. Rong, Q. Zheng, G. Ren, N. Zhang, X. Liu, X. Guo, C. Yang, H. Liu, B. Zhong and Y. Hu, *Adv. Energy Mater.*, 2021, **11**, 2100729.
12 L. H. B. Nguyen, T. Broux, P. S. Camacho, D. Denux, L. Bourgeois, S. Belin, A. Iadecola, F. Fauth, D. Carlier, J. Olchowka, C. Masquelier and L. Croguennec, *Energy Storage Mater.*, 2019, **20**, 324–334.
13 M. Bianchini, F. Fauth, N. Brisset, F. Weill, E. Suard, C. Masquelier and L. Croguennec, *Chem. Mater.*, 2015, **27**, 3009–3020.
14 Y.-U. Park, D.-H. Seo, H. Kim, J. Kim, S. Lee, B. Kim and K. Kang, *Adv. Funct. Mater.*, 2014, **24**, 4603–4614.
15 Y. Qi, L. Mu, J. Zhao, Y. Hu, H. Liu and S. Dai, *Angew. Chem., Int. Ed.*, 2015, **54**, 9911–9916.
16 L. Zhu, H. Wang, D. Sun, Y. Tang and H. Wang, *J. Mater. Chem. A*, 2020, **8**, 21387–21407.
17 K. Chayambuka, M. Jiang, G. Mulder, D. L. Danilov and P. H. L. Notten, *Electrochim. Acta*, 2022, **404**, 139726.
18 N. Eshraghi, S. Caes, A. Mahmoud, R. Cloots, B. Vertruyen and F. Boschini, *Electrochim. Acta*, 2017, **228**, 319–324.
19 F. Li, Y. Zhao, L. Xia, Z. Yang, J. Wei and Z. Zhou, *J. Mater. Chem. A*, 2020, **8**, 12391–12397.
20 L. Zhu, Q. Zhang, D. Sun, Q. Wang, N. Weng, Y. Tang and H. Wang, *Mater. Chem. Front.*, 2020, **4**, 2932–2942.
21 T. Broux, F. Fauth, N. Hall, Y. Chatillon, M. Bianchini, T. Bamine, J. Leriche, E. Suard, D. Carlier, Y. Reynier, L. Simonin, C. Masquelier and L. Croguennec, *Small Methods*, 2019, **3**, 1800215.
22 J. Olchowka, L. H. B. Nguyen, T. Broux, P. Sanz Camacho, E. Petit, F. Fauth, D. Carlier, C. Masquelier and L. Croguennec, *Chem. Commun.*, 2019, **55**, 11719–11722.
23 A. Criado, P. Lavela, C. Pérez-Vicente, G. F. Ortiz and J. L. Tirado, *J. Electroanal. Chem.*, 2020, **856**, 113694.
24 M. Wang, K. Wang, X. Huang, T. Zhou, H. Xie and Y. Ren, *Ceram. Int.*, 2020, **2**, 1–9.

25 C. Guo, J. Yang, Z. Cui, S. Qi, Q. Peng, W. Sun, L.-P. Lv, Y. Xu, Y. Wang and S. Chen, *J. Energy Chem.*, 2022, **65**, 514–523.
26 I. L. Matts, S. Dacek, T. K. Pietrzak, R. Malik and G. Ceder, *Chem. Mater.*, 2015, **27**, 6008–6015.
27 Y. Zhang, S. Guo and H. Xu, *J. Mater. Chem. A*, 2018, **6**, 4525–4534.
28 L. H. B. Nguyen, J. Olchowka, S. Belin, P. Sanz Camacho, M. Duttine, A. Iadecola, F. Fauth, D. Carlier, C. Masquelier and L. Croguennec, *ACS Appl. Mater. Interfaces*, 2019, **11**, 38808–38818.
29 C. Shen, H. Long, G. Wang, W. Lu, L. Shao and K. Xie, *J. Mater. Chem. A*, 2018, **6**, 6007–6014.
30 J. Xun, Y. Zhang and H. Xu, *Inorg. Chem. Commun.*, 2020, **115**, 107884.
31 J. Zhao, L. Mu, Y. Qi, Y. S. Hu, H. Liu and S. Dai, *Chem. Commun.*, 2015, **51**, 7160–7163.
32 A. Mukherjee, T. Sharabani, R. Sharma, S. Okashy and M. Noked, *Batteries Supercaps*, 2020, **3**, 510–518.
33 Y. Qi, L. Mu, J. Zhao, Y.-S. Hu, H. Liu and S. Dai, *J. Mater. Chem. A*, 2016, **4**, 7178–7184.
34 R. Fang, J. Olchowka, C. Pablos, P. S. Camacho, D. Carlier, L. Croguennec and S. Cassaignon, *Batteries Supercaps*, 2022, **5**, e202100179.
35 Y. Qi, J. Zhao, C. Yang, H. Liu and Y.-S. Hu, *Small Methods*, 2019, **3**, 1800111.
36 P. Serras, V. Palomares, J. Alonso, N. Sharma, J. M. López del Amo, P. Kubiak, M. L. Fdez-Gubieda and T. Rojo, *Chem. Mater.*, 2013, **25**, 4917–4925.
37 P. R. Kumar, K. Kubota, Y. Miura, M. Ohara, K. Gotoh and S. Komaba, *J. Power Sources*, 2021, **493**, 229676.
38 D. Semykina, O. Podgornova and N. Kosova, *Mater. Today: Proc.*, 2020, **25**, 497–500.
39 R. Fang, J. Olchowka, C. Pablos, R. Bianchini Nuernberg, L. Croguennec and S. Cassaignon, *ACS Appl. Energy Mater.*, 2022, **5**, 1065–1075.
40 J. Olchowka, L. H. B. Nguyen, E. Petit, P. S. Camacho, C. Masquelier, D. Carlier and L. Croguennec, *Inorg. Chem.*, 2020, **59**, 17282–17290.
41 T. Broux, T. Bamine, F. Fauth, L. Simonelli, W. Olszewski, C. Marini, M. Ménétrier, D. Carlier, C. Masquelier and L. Croguennec, *Chem. Mater.*, 2016, **28**, 7683–7692.
42 J. Rodríguez-Carvajal, *Physica B: Condens. Matter*, 1993, **192**, 55–69.
43 N. Sharma, P. Serras, V. Palomares, H. E. A. Brand, J. Alonso, P. Kubiak, M. L. Fdez-Gubieda and T. Rojo, *Chem. Mater.*, 2014, **26**, 3391–3402.
44 F. D. Hardcastle and I. E. Wachs, *J. Phys. Chem.*, 1991, **95**, 5031–5041.
45 C. J. Antony, A. Aatiq, C. Y. Panicker, M. J. Bushiri, H. T. Varghese and T. K. Manojkumar, *Spectrochim. Acta, Part A*, 2011, **78**, 415–419.
46 J. Olchowka, R. Invernizzi, A. Lemoine, J. Allouche, I. Baraille, D. Flahaut and L. Guerlou-Demourgues, *J. Electrochem. Soc.*, 2020, **167**, 100527.
47 P. Barpanda, R. Dedryvère, M. Deschamps, C. Delacourt, M. Reynaud, A. Yamada and J.-M. Tarascon, *J. Solid State Electrochem.*, 2012, **16**, 1743–1751.
48 J. Olchowka, T. Tailliez, L. Bourgeois, M. A. Dourges and L. Guerlou-Demourgues, *Nanoscale Adv.*, 2019, **1**, 2240–2249.
49 R. Baddour-Hadjean and J. P. Pereira-Ramos, *Chem. Rev.*, 2010, **110**, 1278–1319.
50 A. Criado, P. Lavela, G. Ortiz, J. L. Tirado, C. Pérez-Vicente, N. Bahrou and Z. Edfouf, *Electrochim. Acta*, 2020, **332**, 135502.
51 Y. Cai, X. Cao, Z. Luo, G. Fang, F. Liu, J. Zhou, A. Pan and S. Liang, *Adv. Sci.*, 2018, **2**, 1800680.
52 K. Fujii, T. Fujimori, T. Takamuku, R. Kanzaki, Y. Umebayashi and S. I. Ishiguro, *J. Phys. Chem. B*, 2006, **110**, 8179–8183.
53 C. J. Jafta, X. G. Sun, H. Lyu, H. Chen, B. P. Thapaliya, W. T. Heller, M. J. Cuneo, R. T. Mayes, M. P. Paranthaman, S. Dai and C. A. Bridges, *Adv. Funct. Mater.*, 2021, **31**, 2008708.
54 T. Sugimoto, M. Kikuta, E. Ishiko, M. Kono and M. Ishikawa, *J. Power Sources*, 2008, **183**, 436–440.
55 Z. Tong, Y. Qi, J. Zhao, L. Liu, X. Shen and H. Liu, *Waste Biomass Valorization*, 2020, **11**, 2201–2209.
56 L. H. B. Nguyen, P. Sanz Camacho, T. Broux, J. Olchowka, C. Masquelier, L. Croguennec and D. Carlier, *Chem. Mater.*, 2019, **31**, 9759–9768.
57 W. Papawassiliou, J. P. Carvalho, N. Panopoulos, Y. Al Wahedi, V. K. S. Wadi, X. Lu, K. Polychronopoulou, J. B. Lee, S. Lee, C. Y. Kim, H. J. Kim, M. Katsiotis, V. Tzitzios, M. Karagianni, M. Fardis, G. Papavassiliou and A. J. Pell, *Nat. Commun.*, 2021, **12**, 1–11.
58 L. H. B. Nguyen, A. Iadecola, S. Belin, J. Olchowka, C. Masquelier, D. Carlier and L. Croguennec, *J. Phys. Chem. C*, 2020, **124**, 23511–23522.
59 N. Sharma, P. Serras, V. Palomares, H. E. A. Brand, J. Alonso, P. Kubiak, M. L. Fdez-Gubieda and T. Rojo, *Chem. Mater.*, 2014, **26**, 3391–3402.
60 J.-L. Souquet, *Encyclopedia of Glass Science, Technology, History, and Culture*, Wiley, 2021, pp. 453–463.
61 M. C. Ungureanu, M. Lévy and J. L. Souquet, *Ionics*, 1998, **4**, 200–206.
62 R. B. Nuernberg, *Ionics*, 2020, **26**, 2405–2412.
63 T. Broux, B. Fleutot, R. David, A. Brüll, P. Veber, F. Fauth, M. Courty, L. Croguennec and C. Masquelier, *Chem. Mater.*, 2018, **30**, 358–365.
64 A. Paolella, G. Bertoni, W. Zhu, D. Campanella, A. La Monaca, G. Girard, H. Demers, A. C. Gheorghe Nita, Z. Feng, A. Vijh, A. Guerfi, M. Trudeau, M. Armand and S. A. Krachkovskiy, *J. Am. Chem. Soc.*, 2022, **144**, 3442–3448.
65 A. R. Iarchuk, D. V. Sheptyakov and A. M. Abakumov, *ACS Appl. Energy Mater.*, 2021, **4**, 5007–5014.